remote sensing

MDPI

Technical Note

Planetary Boundary Layer Structure as the Primary Driver of Simulated Impact Multipath in GNSS Radio Occultation

Li Wang and Shengpeng Yang *

Joint Center of Data Assimilation for Research and Application, School of Atmospheric Sciences, Nanjing University of Information Science and Technology, Nanjing 210044, China; 202411010034@nuist.edu.cn
* Correspondence: yangshengp@nuist.edu.cn

Highlights

What are the main findings?

- Approximately 36% of COSMIC-2 RO profiles exhibit simulated impact multipath (SIM).
- More than 70% of SIM cases occur within 0.5 km above the diagnosed planetary boundary layer (PBL) top.

What are the implications of the main findings?

- A clear relationship is revealed between SIM and the strong vertical gradients near PBL structures.
- SIM-based quality control reduces bending angle biases by more than 50%; therefore, the retained dataset better represents the true atmospheric structure.

Abstract

Simulated impact multipath (SIM) occurs when forward operators propagate Global Navigation Satellite System (GNSS) radio occultation (RO) signals through strongly nonspherical atmospheric structures, producing multivalued bending angles that cannot be assimilated directly. In this study, the relationships between SIM and planetary boundary layer (PBL) structures were quantified using COSMIC-2 RO observations and ERA5 reanalysis during two periods (January and July 2022). The results show that SIM affects ~36% of RO profiles, with more than 70% of cases occurring within 0.5 km above the diagnosed PBL top. By defining the simulated impact multipath height (SIMH) as the first detection level of SIM, we found that discarding data below the SIMH reduces bending angle biases by more than half and substantially decreases their scatter. These results provide direct physical evidence linking SIM to strong vertical gradients near PBL structures and establish a quantitative basis for simple, effective quality control, thereby improving weather prediction, particularly in the data-sparse tropical lower troposphere.

Keywords: simulated impact multipath; radio occultation ray paths; GNSS RO; vertical and horizontal gradients of refractivity

Check for updates

Academic Editor: Stephan Havemann

Received: 8 December 2025
Revised: 14 January 2026
Accepted: 17 January 2026
Published: 20 January 2026

Copyright: © 2026 by the authors. Licensee MDPI, Basel, Switzerland. This article is an open access article distributed under the terms and conditions of the Creative Commons Attribution (CC BY) license.

1. Introduction

Global Navigation Satellite System (GNSS) radio occultation (RO) has become a key tool in atmospheric remote sensing, providing high-precision, all-weather observations of the Earth's atmosphere [1]. RO data have been widely applied in climate monitoring [2,3], satellite data calibration [4], and ionospheric research [5] and have significantly improved global numerical weather prediction (NWP), including forecasts of tropical cyclones [6–8].

The launch of the Constellation Observing System for Meteorology, Ionosphere, and Climate-2 (COSMIC-2) in June 2019 marked a major advance in low-latitude RO coverage, with upgraded antenna design, higher sampling rates, and improved open-loop tracking [9–11]. COSMIC-2 now provides a large volume of bending angle, refractivity, temperature, and water vapor profiles over tropical and subtropical oceans.

GNSS RO retrievals are based on detecting signal bending as GNSS signals propagate through the atmosphere to low Earth orbit (LEO) satellites. Bending angles are typically retrieved with wave optics methods under an assumption of spherical symmetry, where the bending angle is treated as a single-valued function of the impact parameter [12–14]. Refractivity profiles are then derived using the Abel transform [1].

In the lower troposphere, however, this symmetry assumption often fails because of strong refractivity gradients. This leads to complex ray propagation phenomena, including multipath and impact multipath [14–16]. These effects degrade the retrieval accuracy. The radio-holographic methods have been developed to mitigate observational multipath and impact multipath [16–19].

In data assimilation, simulated impact multipath (SIM) occurs when bending angles are computed from background fields using observation operators. In such cases (Phenomenon A), the simulated bending angle becomes a multivalued function of the local angular momentum [20]. This violates the assumptions of one-dimensional (1D) Abel-type operators, introduces large errors, and often forces rejection of the affected data [21].

It is crucial to distinguish this phenomenon from another challenge in RO processing, also referred to as "impact multipath" [15,16]. The latter (Phenomenon B) is defined as multivalued ray manifold projections when the effective impact parameter p is used as the coordinate in the mapped space, which occur during the bending angle retrieval process due to strong horizontal refractivity gradients. In contrast, this study (following [20,22]) focuses on Phenomenon A: the simulated bending angle becomes a multivalued function of the local angular momentum, arising during the bending angle assimilation process as a result of strong vertical refractivity gradients.

Recent findings have underscored the importance of effectively utilizing these complex low-level data. Results from the international Radio Occultation Modeling Experiment (ROMEX) [23] demonstrate that assimilating a larger volume of GNSS-RO profiles leads to substantial forecast improvements in temperature, humidity, and wind, with benefits extending from the surface to 300 hPa. Importantly, ROMEX indicates that low-level RO information can meaningfully reduce both scatter and bias in the lower troposphere when available in sufficient volume. This provides strong motivation to retain as much low-level data as possible rather than discard it conservatively [24].

To identify and remove SIM-contaminated profiles, some studies have adopted two-dimensional (2D) ray-tracing operators that explicitly simulate ray paths through heterogeneous atmospheric fields [20,25–27]. Although effective, this approach is computationally expensive and difficult to apply in operational NWP systems. Consequently, most centers continue to use 1D operators for efficiency, despite their limitations under nonsymmetric conditions. This highlights the need for a more efficient, physics-based quality control (QC) strategy to detect SIM profiles without the need for full 2D ray tracing for every case.

SIM not only produces multivalued bending angles but also introduces large errors, especially near the ray perigee [20]. These errors are driven mainly by sharp horizontal refractivity gradients along the ray path and vertical gradients in the radial direction [28,29]. The strongest vertical gradients are typically found near the top of the planetary boundary layer (PBL), where moisture and temperature change rapidly [30]. Previous studies have reported that SIM events often occur at an impact height of ~3.4 km (or ~1.8 km in geometric

height), which roughly corresponds to the PBL height [22], suggesting a close physical connection between SIM and the PBL structure.

This study aimed to address this gap by using a 2D ray-tracing operator to investigate the fine-scale relationship between the PBL structure and the SIM phenomenon. The goal is to provide the physical understanding needed for a targeted, physics-based QC scheme. Such a scheme would allow 1D assimilation systems to safely retain valuable low-level RO data and ultimately improve tropical weather forecasts.

2. Data and Methods

2.1. Data

This study used COSMIC-2 radio occultation (RO) data collected during two 7-day periods: 16–22 January and 16–22 July 2022. COSMIC-2 provided dense RO coverage over the tropical oceanic region (±30° latitude) and helped to fill a long-standing observational gap. We employed the Level-2 "atmPrf" product from the COSMIC Data Analysis and Archival Center (CDAAC) [31], which includes position vectors and azimuth angles at the ray perigee—the point on each RO path closest to the Earth's surface. These perigee-level parameters served as inputs to the 2D ray-tracing observation operator used in this study. In the CDAAC data processing, RO profiles are rejected if the difference in slopes of logarithms of the observational and background bending angle profiles does not exceed 5%, or the retrieved refractivity differs from the background refractivity by more than 50% within 10–40 km [31,32].

The background fields used in the ray-tracing simulations were derived from model-level data of the ECMWF Reanalysis Version 5 (ERA5) and the Committee on Space Research International Reference Atmosphere (CIRA). Compared with its predecessor, ERA-Interim, ERA5 provides substantially improved temporal (hourly) and spatial resolution (31 km horizontally, 137 vertical levels), along with enhanced accuracy in key tropospheric variables such as temperature, wind, and humidity [33,34]. These improvements support a more realistic representation of atmospheric structures across a range of spatial and temporal scales. The Committee on Space Research International Reference Atmosphere (CIRA) model data provide detailed latitudinal mean distributions of the temperature, wind, and geopotential height over isobars from the surface to 120 km, from 80°S to 80°N [35]. We used ERA5 and CIRA variables to compute the atmospheric index of refractivity, which serves as the input for simulating GNSS signal propagation paths in the 2D ray-tracing operator.

2.2. Model

To investigate the relationship between the SIM and the PBL, we first simulated the GNSS RO signal propagation using a two-dimensional (2D) ray-tracing operator. The operator, developed by Zou et al. (1999) [36], solves the following ray trajectory equation:

$$\frac{d^2\vec{r}}{d\tau^2} = n\nabla n \tag{1}$$

where $\vec{r}$ is the three-dimensional (3D) position vector pointing from the center of the Earth to any point on the simulated ray trajectory. n is the atmospheric index of refractivity, and τ is related to the atmospheric index of refractivity (n) and the ray length (s), $d\tau = ds/dn$. For ease of calculation, the second-order ordinary differential (1) is decomposed into first-order ordinary differential equations:

$$\begin{cases} \frac{d\vec{r}}{d\tau} = \vec{y} \\ \frac{d\vec{y}}{d\tau} = n\nabla n \end{cases} \tag{2}$$

where $\vec{y}$ represents the tangent direction at a point on the ray. The refractive index n is computed from the atmospheric refractivity N as follows:

$$n = N \times 10^{-6} + 1 \tag{3}$$

The refractivity N depends on temperature and water vapor [1,13,14,37]:

$$N = a_1 \frac{P}{T} + a_2 \frac{P_W}{T^2} \tag{4}$$

where P is the pressure (unit: hPa), P_w is the water vapor pressure (unit: hPa), and T is the temperature (unit: K). The constants are a_1 = 77.6 K/hPa and a_2 = 3.73 × 10^5 K^2/hPa. ERA5 provides atmospheric fields from the surface to the ERA5 model top (~77–80 km). For numerical completeness of the 2D ray-tracing integration, we extend the profile to 120 km using CIRA and set refractivity to zero above 120 km. The ERA5–CIRA fields are vertically stitched with smoothing across the transition and interpolated onto the ray-tracing grid (2 km horizontal step; 100 m vertical spacing) before integration. The CIRA extension is used solely to furnish a continuous upper-atmospheric profile for the integrator and is not intended to influence lower-tropospheric SIM diagnostics. ERA5 fields are used as the background input to drive the 2D ray-tracing operator. The resulting simulated bending angles are compared against COSMIC-2 observations to diagnose deviations associated with multipath-favorable refractivity structures.

The ray path is integrated bidirectionally from the perigee toward the GNSS and LEO satellites using a horizontal step size of 2 km and a vertical resolution of 100 m. At each integration step, the local angular momentum (p_θ, also referred to as horizontal momentum) is calculated as follows:

$$p_\theta = rn(r)sin\phi \tag{5}$$

where ϕ is the angle between the local radius vector and the tangent direction of the ray. At the perigee, $\phi = 90^\circ$, this value is $a_0 = r_0 n(r_0)$. Following Yang and Zou (2021) [22], we use this perigee momentum value (a_0) as the diagnostic coordinate for indexing the ray. The "perigee impact height" is defined as this a_0 minus the radius of curvature of the Earth. The bending angle is defined as the angle between the tangent vector at the GNSS satellite ($\vec{t_G}$) and that at the LEO satellite ($\vec{t_L}$). The geometrical expression is shown below:

$$\alpha_{2D} = \angle\left(\vec{t_G}, \vec{t_L}\right) \tag{6}$$

2.3. PBLH Diagnosis

The planetary boundary layer height (PBLH) was determined using the refractivity gradient method, which locates the PBL top at the altitude of the minimum negative vertical refractivity gradient [30,38]. This altitude corresponds to the sharp transition in temperature and humidity at the PBL top. To ensure that the lowest measurements of the profiles fall within the PBL, only profiles with a lowest penetration height below 500 m were retained in the analysis examining the relationship between the PBL and SIM. We use ERA5 profiles to calculate the PBLHs.

3. Results

3.1. Simulated Impact Multipath Phenomenon Identification

In a spherically symmetric atmosphere, Bouguer's law implies that the local angular momentum (p_θ, Equation (5)) is conserved along the ray trajectory. When horizontal inhomogeneities (i.e., $n/\partial\theta \neq 0$) break this symmetry, p_θ is no longer conserved [15],

which can lead to projection ambiguities in retrieval [16]. A different phenomenon occurs when strong vertical gradients (i.e., super-refraction) are present. This can cause geometric ray crossing (caustics), where different simulated rays, originating from adjacent perigee coordinates (a_0), physically intersect. This is the phenomenon we (and [22,39]) refer to as simulated impact multipath (SIM). In such cases, the simulated bending angle becomes a multivalued function of the local angular momentum, as shown in Zou et al. (2019) [20].

We define the simulated impact multipath height (SIMH) as the perigee altitude at which bending angles first become multivalued. Below the SIMH, the simulated bending angles diverge substantially from the observed bending angles and should be excluded prior to assimilation [20]. To be consistent with common practice in meteorology, we employ the horizontal and vertical refractivity gradients defined in a local Cartesian coordinate system ($\partial N/\partial x$ and $\partial N/\partial z$) [22] rather than that in polar coordinates ($\partial N/\partial \theta$ and $\partial N/\partial r$) [28,29] (Figure 1).

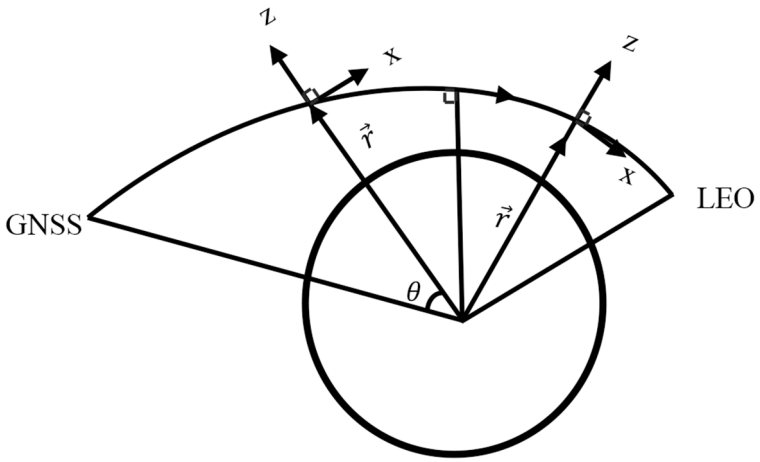

Figure 1. The geometry of the radio occultation coordinates.

We illustrate the SIM phenomenon using two representative COSMIC-2 events (Figure 2). In RO1 (Figure 2, left), SIM occurs at perigee impact heights of 3.1 – 3.3 km. The simulated bending angle becomes a multivalued function of the perigee coordinate, with abrupt changes exceeding 0.06 rad (Figure 2a). This anomaly coincides precisely with the region of steep vertical refractivity gradients (Figure 2g), where gradients approach or exceed -140 N-unit/km, indicating super-refraction. This confirms the findings of Yang and Zou (2021) [22] and the reviewer's insight that strong vertical gradients are the direct physical cause of this geometric multivaluedness. The large deviations in local angular momentum along the path ($|\, p_\theta(s) - a_0 \,|$; Figure 2c) and the strong horizontal gradients (Figure 2e,i) are physically associated features of the complex 3D PBL structure, which modulate this effect but are not the primary driver of this specific geometric phenomenon.

In contrast, RO2 (Figure 2, right) shows no SIM phenomenon. The bending angle remains single-valued (Figure 2b), the local angular momentum is nearly constant along the ray trajectory (Figure 2d), the horizontal and vertical refractivity gradients are smooth (Figure 2f,h), and the variations in the gradient terms remain small (Figure 2j,l). The SIMH (the blue lines in Figure 2i,k) in RO1 lies slightly above the diagnosed PBLH (the red lines in Figure 2i,k), highlighting the physical link between SIM and sharp refractivity gradients near the PBL top.

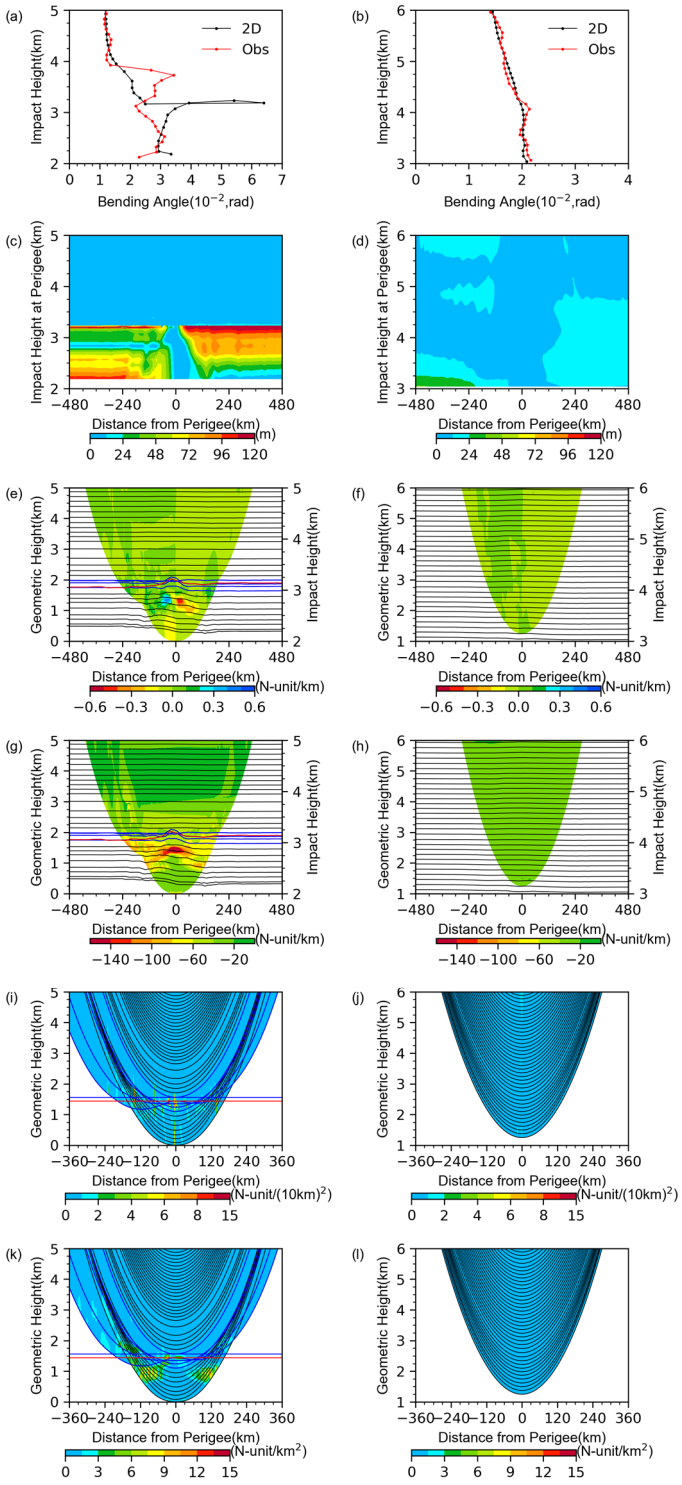

Figure 2. COSMIC-2 RO event 1 (RO1, left) and event 2 (RO2, right). (**a**,**b**) Bending angle profiles from COSMIC-2 retrievals (red) and 2D ray-tracing simulations (black). (**c**,**d**) Absolute differences between local angular momentum along the ray paths and at perigee ($|p_\theta - a_0|$; m). (**e**,**f**) Horizontal refractivity gradients. (**g**,**h**) Vertical refractivity gradients. (**i**,**j**) Variations in horizontal refractivity gradients along ray paths ($|\partial^2 N/\partial x \partial s|$, N-unit/(10 km)^2). (**k**,**l**) Variations in vertical refractivity gradients along ray paths ($|\partial^2 N/\partial z \partial s|$, N-unit/km^2). The black solid lines mark the ray impact (**e**–**h**) and geometric heights (**i**–**l**); the blue lines denote simulated impact multipath (SIM) occurrence; the red lines mark the planetary boundary layer height (PBLH) at perigee (**e**,**g**); and the blue and red horizontal lines indicate the SIM height (SIMH) and PBLH, respectively (**i**,**k**). RO1 occurred at 0526 UTC on 16 January 2022 (68.94°E, 13.96°N), and RO2 occurred at the same time (119.94°E, 28.27°N).

3.2. Statistical Results

The preceding analysis suggests a close connection between the PBL and SIM. We now examined this link quantitatively through statistical comparisons for two contrasting periods: 16–22 January 2022 (winter monsoon) and 16–22 July 2022 (summer monsoon). The results are summarized in Figures 3–9.

Figure 3 maps COSMIC-2 occultation locations for 16–22 January and 16–22 July 2022, with and without SIM. Some minor differences in the spatial distributions of SIM phenomena between January and July. SIM occurs more frequently over the Arabian Sea and Bay of Bengal during 16–22 January (Figure 3a) than during 16–22 July (Figure 3b). Conversely, SIM is more widespread in the eastern Pacific during 16–22 July (Figure 3b) than during 16–22 January (Figure 3a). These patterns are broadly consistent with established "ducting regions" in the subtropical oceans between 30°S and 30°N [40,41] and with the governing circulation and boundary-layer structure in those basins [42–46].

In January, profiles with SIM exhibited substantially larger mean deviations in the local angular momentum differences ($|p_\theta - a_0|$) than those without SIM, with correspondingly higher standard deviations (Figure 4a,b). This finding indicates that SIM events are characterized by strong distortions of ray trajectories relative to their perigee geometry. Moreover, SIM cases were associated with markedly enhanced vertical refractivity gradients ($|\partial N/\partial z|$, Figure 4e) and vertical gradient variability ($\left|\partial^2 N/\partial z \partial s\right|$; Figure 4i), confirming the primary link to strong vertical structures (super-refraction). These cases also show enhanced horizontal refractivity gradients ($|\partial N/\partial x|$, Figure 4c,g), which is expected, as the PBL top is a dynamically active 3D region where strong vertical and horizontal gradients are often physically associated.

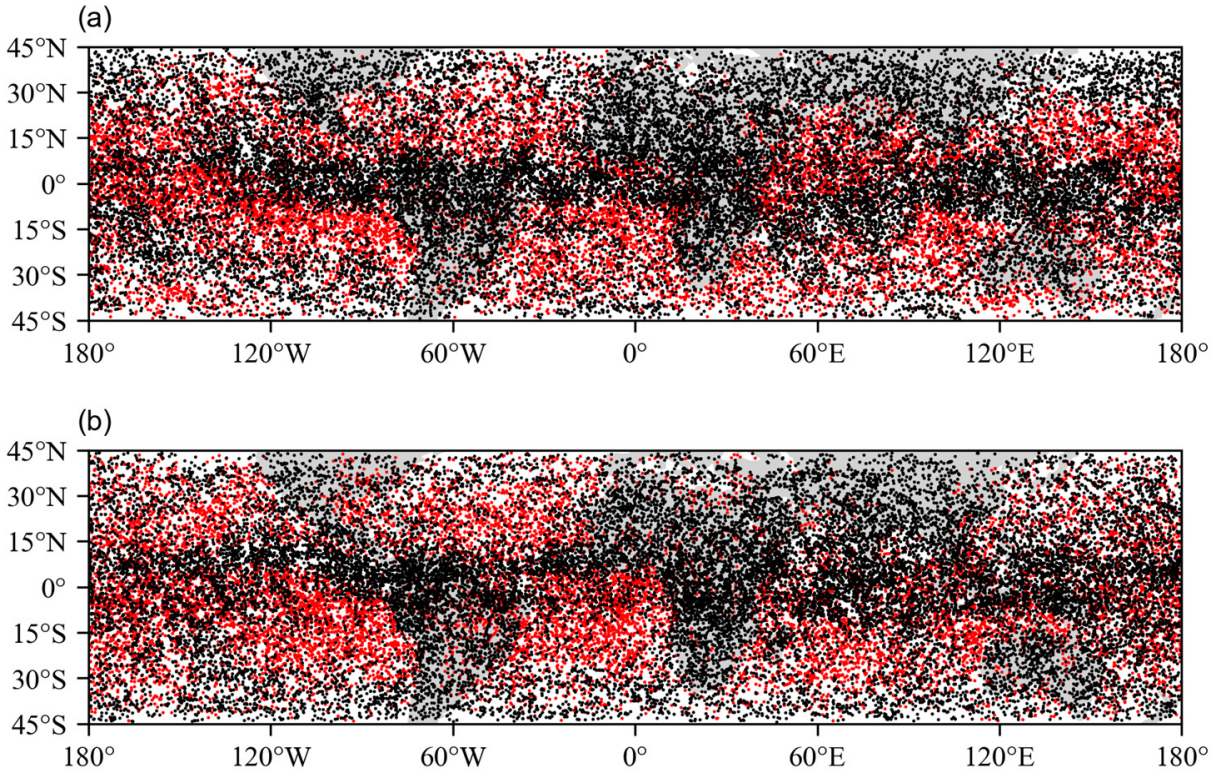

Figure 3. Spatial distributions with (red dots) and without (black dots) SIM phenomena during (**a**) 16–22 January 2022 and (**b**) 16–22 July 2022.

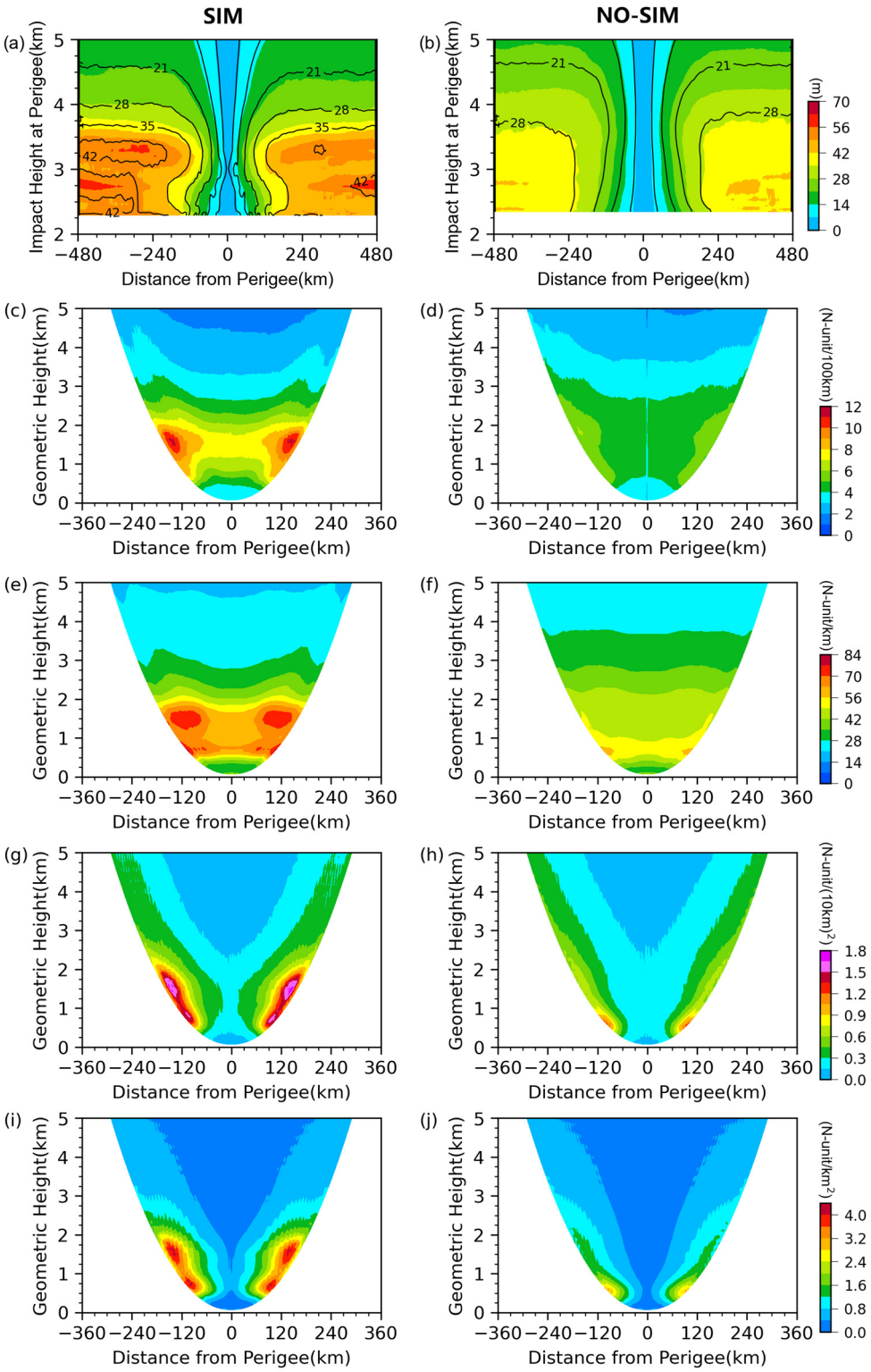

Figure 4. The averages (colored shading) and standard deviations (contour lines) of local angular momentum differences ($|p_\theta - a_0|$, m) (**a**,**b**), averages of the absolute values of horizontal refractivity gradients ($|\partial N/\partial x|$, N-unit/100 km) (**c**,**d**) and vertical refractivity gradients ($|\partial N/\partial z|$, N-unit/km) (**e**,**f**), variations in the horizontal refractivity gradients ($|\partial^2 N/\partial x \partial s|$, N-unit/(10 km)^2) (**g**,**h**) and vertical refractivity gradients($|\partial^2 N/\partial z \partial s|$, N-unit/km^2) (**i**,**j**) along the path of the rays under conditions of presence (left) and absence (right) of SIM phenomena for 16–22 January 2022.

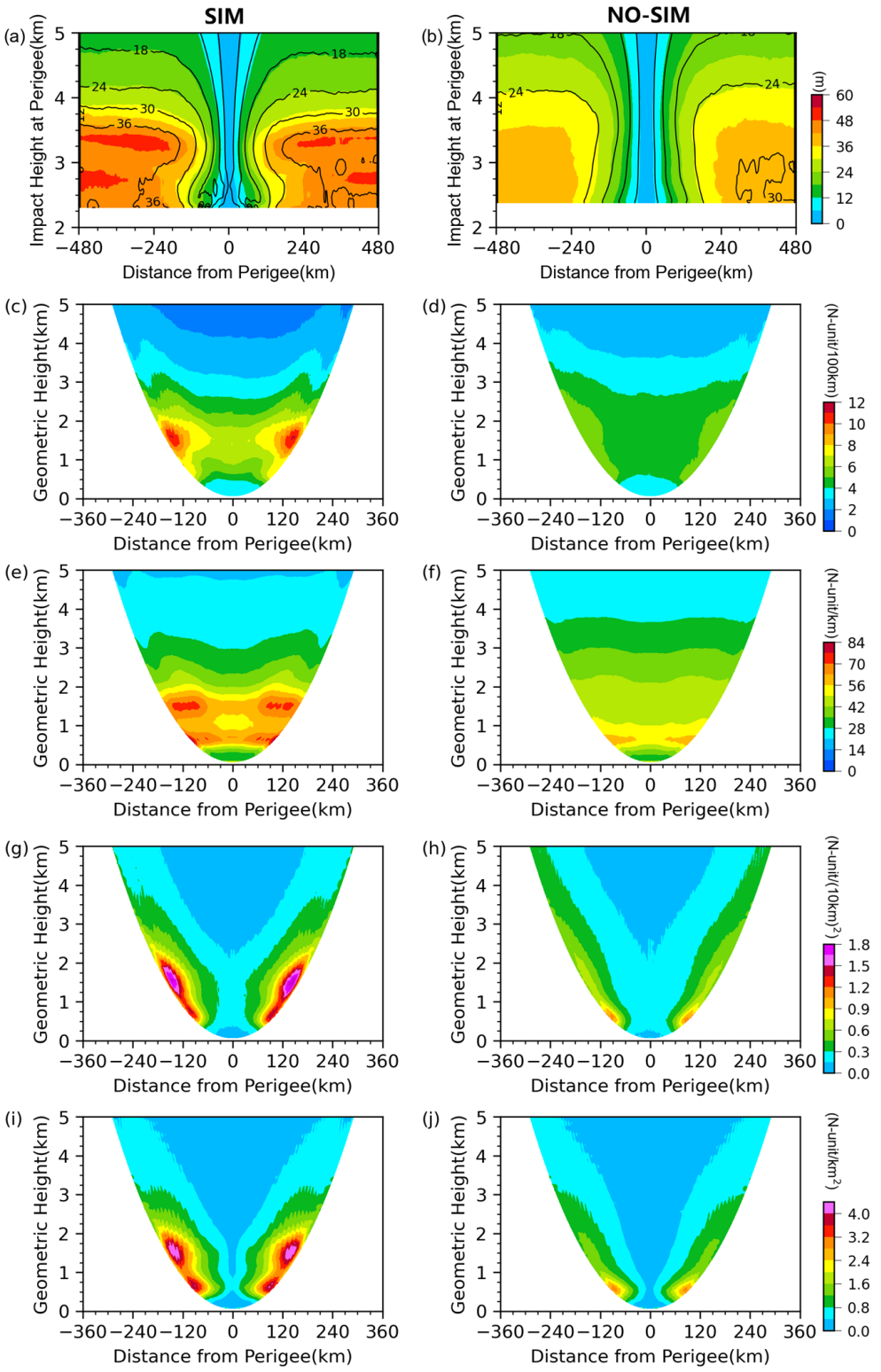

Figure 5. The averages (colored shading) and standard deviations (contour lines) of local angular momentum differences ($|p_\theta - a_0|$, m) (**a,b**), averages of the absolute values of horizontal refractivity gradients ($|\partial N/\partial x|$, N-unit/100 km) (**c,d**) and vertical refractivity gradients ($|\partial N/\partial z|$, N-unit/km) (**e,f**), variations in the horizontal refractivity gradients ($|\partial^2 N/\partial x \partial s|$, N-unit/(10 km)^2) (**g,h**) and vertical refractivity gradients($|\partial^2 N/\partial z \partial s|$, N-unit/km^2) (**i,j**) along the path of the rays under conditions of presence (left) and absence (right) of SIM phenomena for 16–22 July 2022.

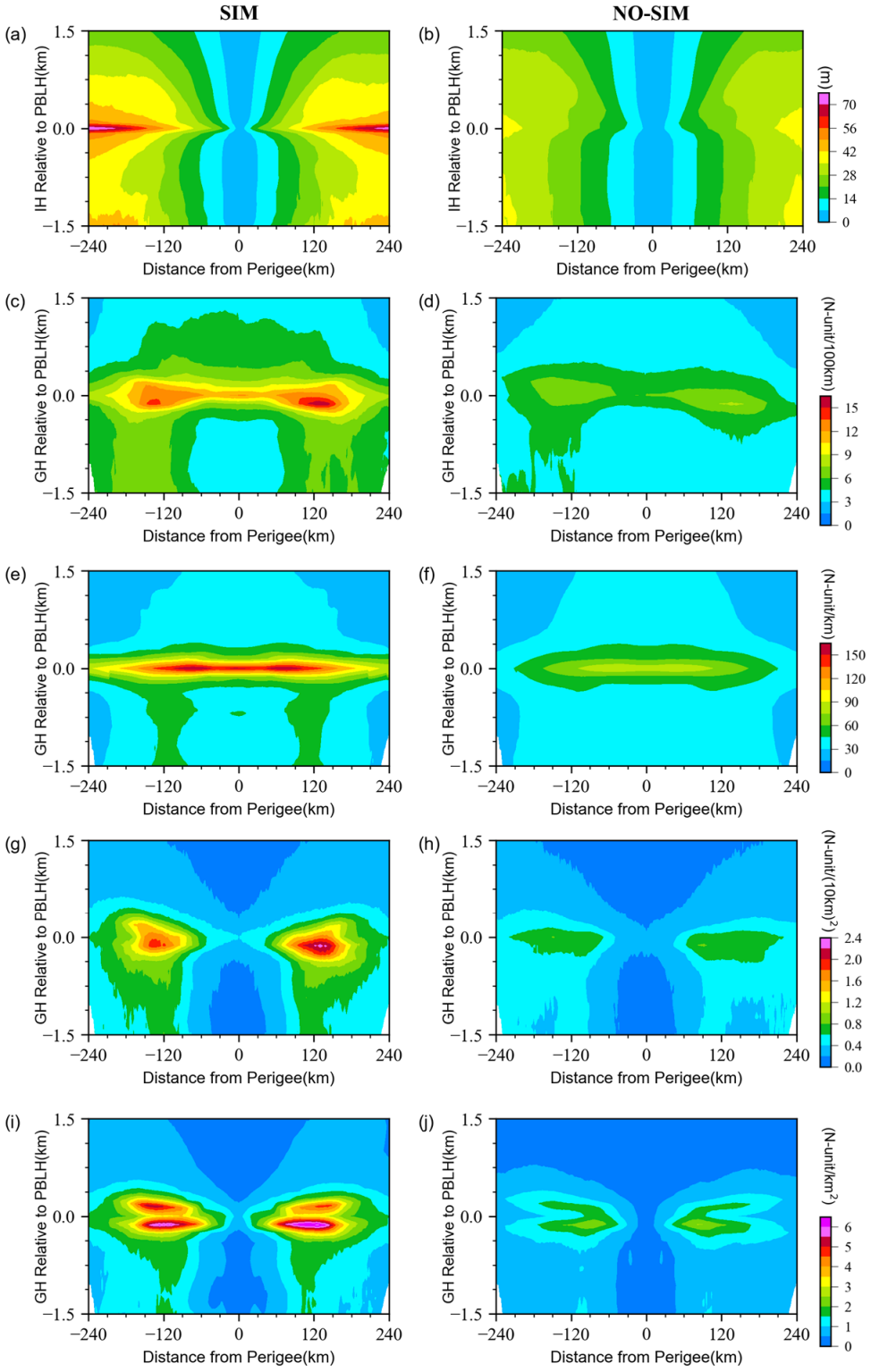

Figure 6. The averages (colored shading) and standard deviations (contour lines) of local angular momentum differences ($|p_\theta - a_0|$, m) (**a**,**b**), averages of the absolute values of horizontal refractivity gradients ($|\partial N/\partial x|$, N-unit/100 km) (**c**,**d**) and vertical refractivity gradients ($|\partial N/\partial z|$, N-unit/km) (**e**,**f**), variations in the horizontal refractivity gradients ($|\partial^2 N/\partial x \partial s|$, N-unit/(10 km)^2) (**g**,**h**) and vertical refractivity gradients($|\partial^2 N/\partial z \partial s|$, N-unit/km^2) (**i**,**j**) along the path of the rays under conditions of presence (left) and absence (right) of SIM phenomena for 16–22 January 2022. The height is expressed relative to the PBLH.

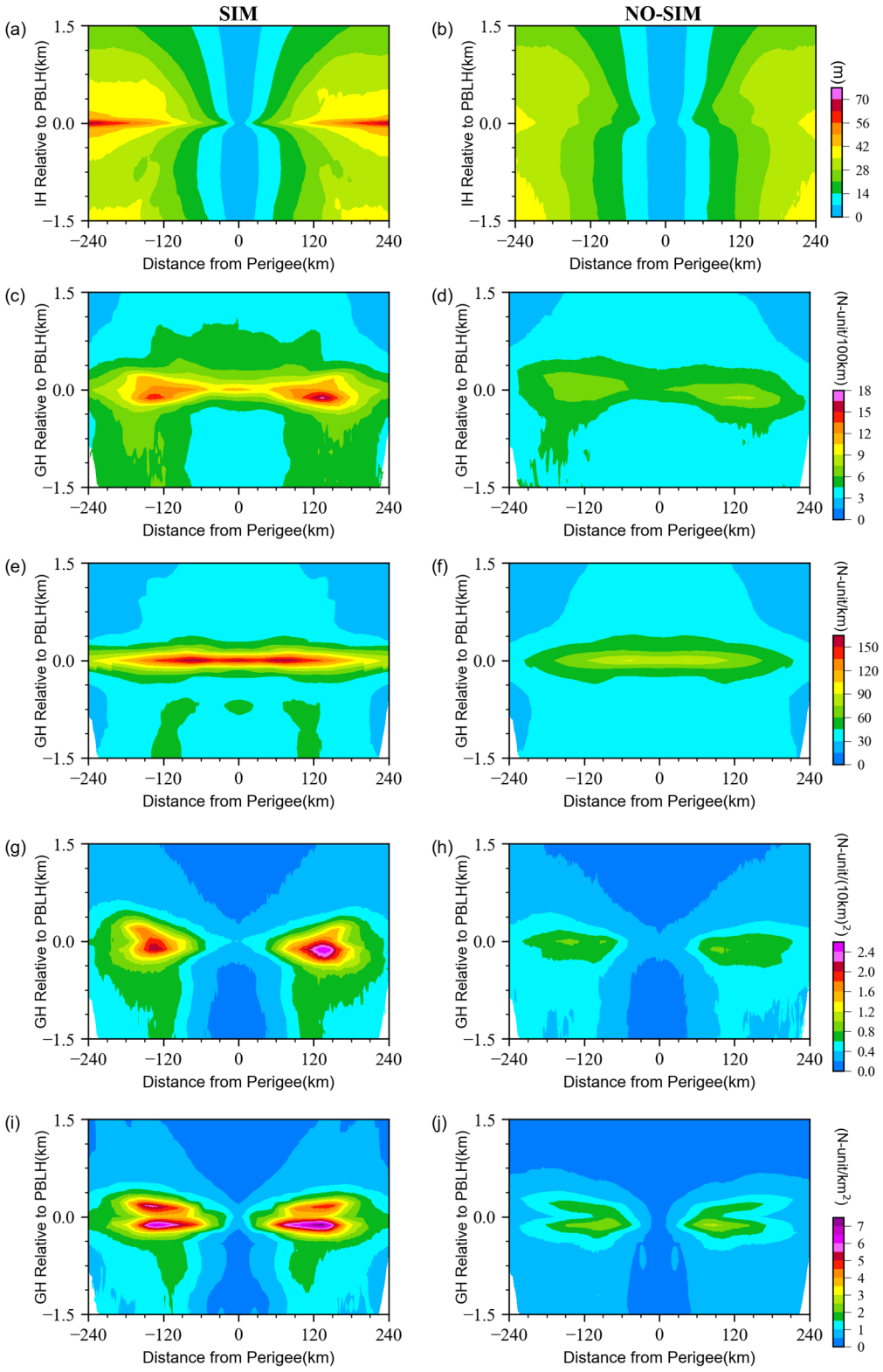

Figure 7. The averages (colored shading) and standard deviations (contour lines) of local angular momentum differences ($|p_\theta - a_0|$, m) (**a**,**b**), averages of the absolute values of horizontal refractivity gradients ($|\partial N/\partial x|$, N-unit/100 km) (**c**,**d**) and vertical refractivity gradients ($|\partial N/\partial z|$, N-unit/km) (**e**,**f**), variations in the horizontal refractivity gradients ($|\partial^2 N/\partial x \partial s|$, N-unit/(10 km)^2) (**g**,**h**) and vertical refractivity gradients($|\partial^2 N/\partial z \partial s|$, N-unit/km^2) (**i**,**j**) along the path of the rays under conditions of presence (left) and absence (right) of SIM phenomena for 16–22 July 2022. The height is expressed relative to the PBLH.

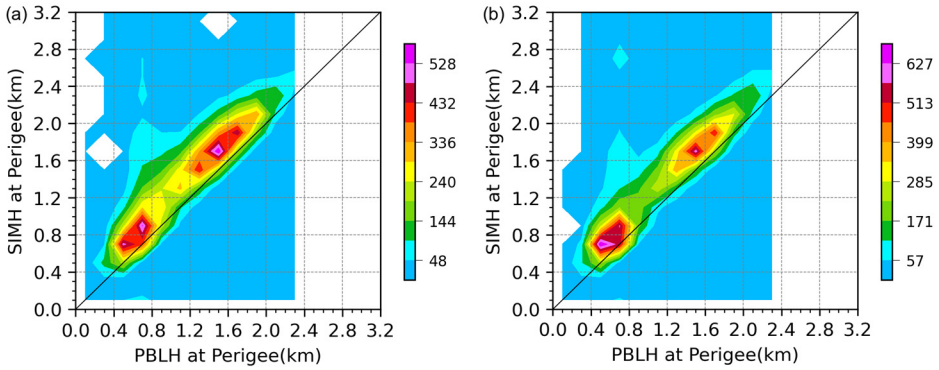

Figure 8. Distribution of SIMH and PBLH data counts in perigees within a 0.2 km × 0.2 km box from (**a**) 16–22 January 2022 and (**b**) 16–22 July 2022.

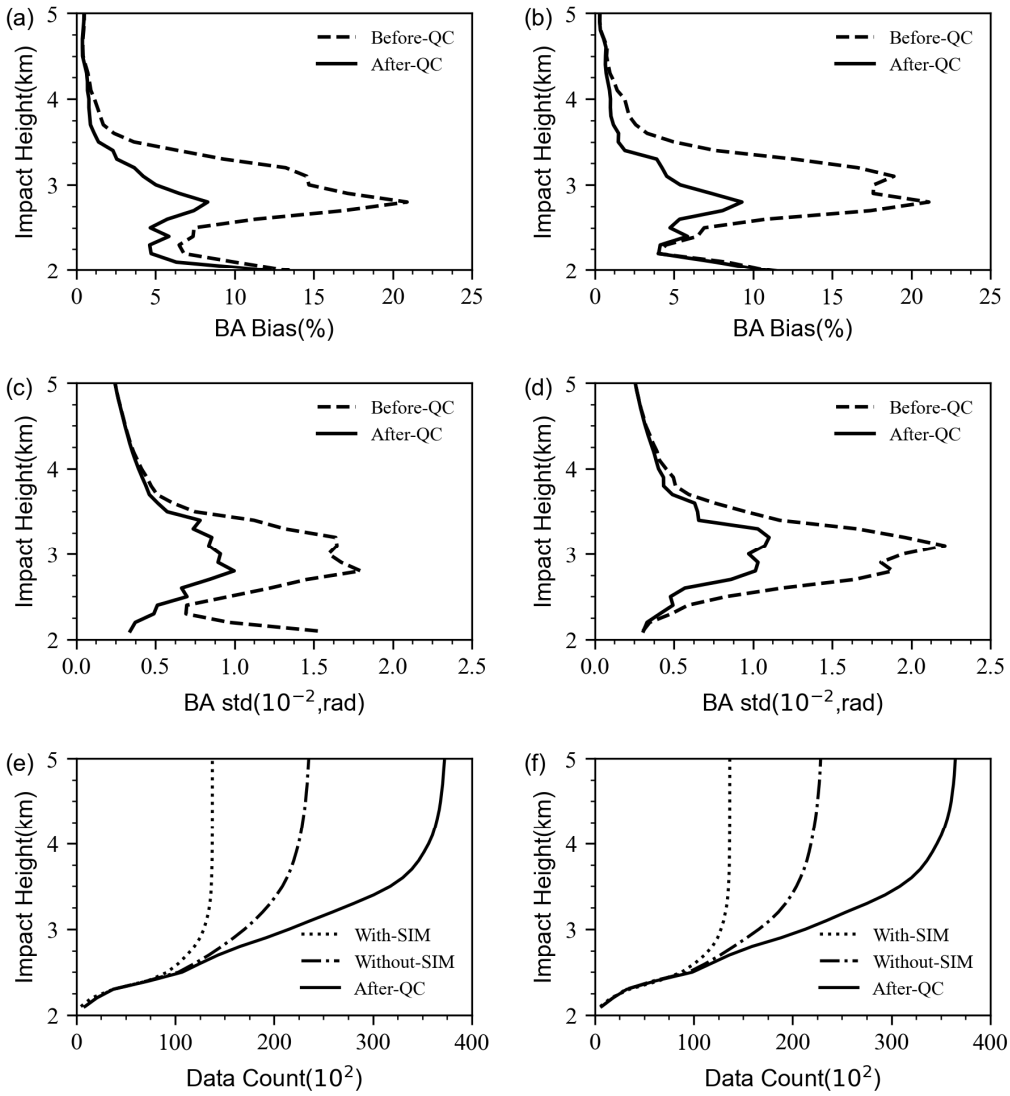

Figure 9. Vertical distributions of (**a**,**b**) mean fractional differences (%) between two-dimensional (2D) simulations and COSMIC-2 bending angles before (dashed) and after QC (solid), (**c**,**d**) the standard deviations of 2D simulated bending angles, and (**e**,**f**) data counts for cases with SIM (dotted), without SIM (dash–dot), and after QC (solid), during 16–22 January (**a**–**c**) and 16–22 July (**d**–**f**) 2022.

Similar results were observed for July (Figure 5), when strong convection and deep PBLs dominated over tropical oceans. Again, the SIM cases displayed larger $|p_\theta - a_0|$ values and variability (Figure 5a,b), enhanced horizontal and vertical refractivity gradients (Figure 5c–f), and larger along-path fluctuations (Figure 5g,j). The similarity of the January and July statistics indicates that SIM occurrence is a robust phenomenon across different seasons and meteorological regimes, although the absolute magnitudes of variabilities of refractivity gradients were generally greater in July because of stronger convection and moisture variability.

To demonstrate the close relationship between the PBL and SIM, Figures 6 and 7 present the distributions of the variables shown in Figures 4 and 5 relative to the PBLH. The results for January and July are highly similar. During SIM events, strong transition zones of $|p_\theta - a_0|$ (Figures 6a,b and 7a,b) and of the horizontal (Figures 6c,d and 7c,d) and vertical refractivity gradients (Figures 6e,f and 7e,f) are observed near the PBL top, with their magnitudes reaching maximum values at the PBLH. Above and below the PBLH, there exist large-value regions for horizontal (Figures 6g,h and 7g,h) and vertical gradient (Figures 6i,j and 7i,j) variability. This further confirms the strong connection between the PBLH and SIM events.

We further analyzed the relative positions of the SIMH and the diagnosed PBLH. Figure 8 shows that the majority of the SIMH values clustered near the PBLH, with more than 70% of the SIM events occurring within 0.5 km of the diagnosed PBLH in both January (70.2%; Figure 8a) and July (70.7%; Figure 8b). Within this range, 34.5% (January) and 34.7% (July) of the SIMHs occurred only 0–0.2 km above the PBLHs. In both periods, the SIMH data counts exhibit local maxima at geometric heights of 0.8 km and 1.7 km, while the PBLH data counts show local maxima at 0.6 km and 1.5 km. These statistics indicate that the vast majority of SIMH values are slightly higher than the PBLH, which is related to the structure of the refractivity gradient transition zone at the PBL top (Figures 6 and 7). SIM events already begin to occur above the PBL under the influence of strong refractivity gradients, with their most pronounced manifestation occurring at the PBLH.

In the 2D occultation plane, the along-track change in bending angle depends on both the horizontal and vertical refractivity gradients [20,29]. Consequently, SIM induced by strong refractivity gradients not only transforms the simulated bending angle into a multivalued function of the local angular momentum but also leads to a dramatic increase in the simulated bending angle magnitude. The assimilation of GNSS RO data requires the simulated bending angle to be a single-valued function of the local angular momentum; therefore, data affected by SIM phenomena must be removed in advance. Finally, we assessed the impact of removing data below the SIMH as a quality control (QC) measure using data simulated with the 2D ray-tracing operator (Figure 9), demonstrating the importance of SIM-related quality control. After QC, the mean fractional differences between the COSMIC-2 retrievals and 2D simulations (Figure 9a,b) decreased substantially, with peak biases reduced from ~20% to less than 10%. The standard deviations of the bending angles were also reduced (Figure 9c,d), indicating improved internal consistency of the dataset. In January, 13,755 occultations were flagged with SIM compared with 24,279 retained (Figure 9e), whereas in July, 13,652 were flagged compared with 23,585 retained (Figure 9f). The clear reduction in both random scatter and systematic B–O bias after QC demonstrates the importance of removing data below the SIMH. By excluding multipath-contaminated observations, the retained dataset better represents the true atmospheric structure and is more suitable for assimilation into numerical weather prediction models.

4. Conclusions

In this study, the occurrence and physical basis of simulated impact multipath (SIM) in GNSS RO bending angle data were quantitatively investigated using COSMIC-2 observations and 2D ray-tracing simulations from 16 to 22 January and 16 to 22 July 2022. We found that SIM affects a substantial fraction of occultations, accounting for 36.2% of 38,034 profiles in January and 36.7% of 37,237 profiles in July, respectively.

The results demonstrate that SIM occurrence is closely linked to sharp vertical atmospheric structures at the planetary boundary layer (PBL) top. The primary driver for the observed geometric multivalue is the presence of strong vertical gradients leading to super-refraction. The associated horizontal gradients, which are characteristic of the 3D PBL structure, modulate the extent and complexity of these events. By defining the simulated impact multipath height (SIMH) as the perigee level where SIM was first detected, we found that most of the SIMH values (70.2% in January and 70.7% in July) occurred within 0.5 km above the diagnosed PBL height, confirming that the PBL top is the dominant environment for SIM generation.

Finally, we assessed the effectiveness of a SIMH-based quality control (QC) strategy. Removing data below the SIMH substantially reduced the biases between the COSMIC-2 retrievals and simulations: the peak mean B–O difference decreased from ~20% to <10%, and the associated scatter was reduced by nearly half. Although this filtering discarded a significant number of low-level occultations (e.g., 13,755 flagged vs. 24,279 retained in January; 13,652 flagged vs. 23,585 retained in July), the retained dataset exhibits improved consistency and representativeness of the actual atmospheric structure.

These results provide quantitative evidence of the strong physical connection between SIM (driven by super refraction) and the PBL, establishing the basis for more effective QC of GNSS RO data. This work is complementary to studies focusing on horizontal-gradient-induced retrieval errors (e.g., [16]). By mitigating geometric multipath contamination associated with strong vertical gradients, especially in the data-sparse tropical lower troposphere, SIMH-based filtering enhances the reliability of RO observations for assimilation in numerical weather prediction. Future work will focus on extending these findings to develop a computationally efficient and broadly applicable QC that does not rely on a 2D observation operator, explicitly incorporates model PBL diagnostics, and systematically evaluates their forecast impacts.

Author Contributions: Conceptualization, S.Y.; data curation, L.W.; formal analysis, L.W. and S.Y.; funding acquisition, S.Y.; investigation, L.W. and S.Y.; methodology, S.Y.; project administration, S.Y.; resources, S.Y.; writing—original draft, L.W.; writing—review and editing, S.Y. All authors have read and agreed to the published version of the manuscript.

Funding: This work was supported by the National Natural Science Foundation of China (42275005), the project of Civil Aerospace Preliminary Research (D010404), the Key Research and Development Program of Guangxi (GuiKe AB25069131), and the Postgraduate Research & Practice Innovation Program of Jiangsu Province (KYCX25_1591).

Data Availability Statement: The COSMIC-2 RO data used in this study can be downloaded at: https://data.cosmic.ucar.edu/gnss-ro/cosmic2/nrt/level2/2022/ (accessed on 1 March 2024). The ECMWF ERA5 reanalysis data used in this study can be downloaded at: https://apps.ecmwf.int/data-catalogues/era5/?stream=oper&levtype=ml&expver=1&month=jan&year=2022&type=an&class=ea (accessed on 5 March 2024). The CIRA data used in this study can be downloaded directly at: https://data.ceda.ac.uk/badc/cira/data/ (accessed on 10 March 2024).

Acknowledgments: We are particularly grateful to Michael E. Gorbunov for his valuable suggestions on an earlier version of this manuscript.

Conflicts of Interest: The authors declare no conflicts of interest.

Abbreviations

The following abbreviations are used in this manuscript:

SIM	Simulated Impact Multipath
SIMH	Simulated Impact Multipath Height
GNSS	Global Navigation Satellite System
RO	Radio Occultation
PBL	Planetary Boundary Layer
PBLH	Planetary Boundary Layer Height
COSMIC-2	Constellation Observing System for Meteorology, Ionosphere, and Climate-2
LEO	Low Earth Orbit
1D	One-Dimensional
2D	Two-Dimensional
3D	Three-Dimensional
QC	Quality Control
ROMEX	Radio Occultation Modeling Experiment
ERA5	European Centre for Medium-Range Weather Forecasts Reanalysis Version 5
CIRA	Committee on Space Research International Reference Atmosphere

References

1. Kursinski, E.R.; Hajj, G.A.; Bertiger, W.I.; Leroy, S.S.; Meehan, T.K.; Romans, L.J.; Schofield, J.T.; McCleese, D.J.; Melbourne, W.G.; Thornton, C.L.; et al. Initial results of radio occultation observations of Earth's atmosphere using the Global Positioning System. *Science* **1996**, *271*, 1107–1110. [CrossRef]
2. Innerkofler, J.; Kirchengast, G.; Schwärz, M.; Pock, C.; Jäggi, A.; Andres, Y.; Marquardt, C. Precise orbit determination for climate applications of GNSS Radio Occultation including uncertainty estimation. *Remote Sens.* **2020**, *12*, 1180. [CrossRef]
3. Gleisner, H.; Ringer, M.A.; Healy, S.B. Monitoring global climate change using GNSS Radio Occultation. *npj Clim. Atmos. Sci.* **2022**, *5*, 6. [CrossRef]
4. Ferretti, A.; Fumagalli, A.; Passera, E.; Rucci, A. InSAR data calibration in wide area processing. In Proceedings of the 2022 IEEE International Geoscience and Remote Sensing Symposium (IGARSS), Kuala Lumpur, Malaysia, 17–22 July 2022; pp. 5101–5104. [CrossRef]
5. Wu, D.L. Ionospheric S4 Scintillations from GNSS Radio Occultation (RO) at Slant Path. *Remote Sens.* **2020**, *12*, 2373. [CrossRef]
6. Anthes, R.A. Exploring Earth's atmosphere with radio occultation: Contributions to weather, climate and Space Weather. *Atmos. Meas. Tech.* **2011**, *4*, 1077–1103. [CrossRef]
7. Bai, W.; Deng, N.; Sun, Y.; Du, Q.; Xia, J.; Wang, X.; Meng, X.; Zhao, D.; Liu, C.; Tan, G.; et al. Applications of GNSS-RO to numerical weather prediction and tropical cyclone forecast. *Atmosphere* **2020**, *11*, 1204. [CrossRef]
8. Wang, L.; Yang, S.; Lin, L. Tropical cyclone planetary boundary layer heights derived from GPS radio occultation over the western Pacific Ocean. *Remote Sens.* **2022**, *14*, 6110. [CrossRef]
9. Ho, S.-P.; Zhou, X.; Shao, X.; Zhang, B.; Adhikari, L.; Kireev, S.; He, Y.; Yoe, J.G.; Xia-Serafino, W.; Lynch, E. Initial assessment of the COSMIC-2/FORMOSAT-7 neutral atmosphere data quality in NESDIS/STAR using in situ and satellite data. *Remote Sens.* **2020**, *12*, 4099. [CrossRef]
10. Chen, S.-Y.; Liu, C.-Y.; Huang, C.-Y.; Hsu, S.-C.; Li, H.-W.; Lin, P.-H.; Cheng, J.-P.; Huang, C.-Y. An analysis study of FORMOSAT-7/COSMIC-2 radio occultation data in the troposphere. *Remote Sens.* **2021**, *13*, 717. [CrossRef]
11. Schreiner, W.S.; Weiss, J.P.; Anthes, R.A.; Braun, J.; Chu, V.; Fong, J.; Hunt, D.; Kuo, Y.-H.; Meehan, T.; Serafino, W.; et al. COSMIC-2 Radio Occultation Constellation: First Results. *Geophys. Res. Lett.* **2020**, *47*, e2019GL086841. [CrossRef]
12. Fjeldbo, G.; Kliore, A.J.; Eshleman, V.R. The neutral atmosphere of Venus as studied with the Mariner V Radio Occultation experiments. *Astron. J.* **1971**, *76*, 123. [CrossRef]
13. Kursinski, E.R.; Hajj, G.A.; Schofield, J.T.; Linfield, R.P.; Hardy, K.R. Observing Earth's atmosphere with radio occultation measurements using the Global Positioning System. *J. Geophys. Res. Atmos.* **1997**, *102*, 23429–23465. [CrossRef]
14. Kursinski, E.R.; Hajj, G.A.; Leroy, S.S.; Herman, B. The GPS Radio Occultation Technique. *Terr. Atmos. Ocean. Sci.* **2000**, *11*, 053. [CrossRef]
15. Gorbunov, M.E.; Lauritsen, K.B.; Leroy, S.S. Application of Wigner distribution function for analysis of radio occultations. *Radio Sci.* **2010**, *45*, RS6011. [CrossRef]
16. Gorbunov, M.; Kirchengast, G.; Lauritsen, K.B. Generalized canonical transform method for radio occultation sounding with improved retrieval in the presence of horizontal gradients. *Atmos. Meas. Tech.* **2021**, *14*, 853–867. [CrossRef]

17. Gorbunov, M.E. Radio-holographic analysis of Microlab-1 radio occultation data in the lower troposphere. *J. Geophys. Res. Atmos.* **2002**, *107*, ACK 7-1–ACK 7-10. [CrossRef]
18. Jensen, A.S.; Lohmann, M.S.; Benzon, H.; Nielsen, A.S. Full spectrum inversion of radio occultation signals. *Radio Sci.* **2003**, *38*, 1040. [CrossRef]
19. Sokolovskiy, S.; Rocken, C.; Schreiner, W.; Hunt, D. On the uncertainty of radio occultation inversions in the lower troposphere. *J. Geophys. Res. Atmos.* **2010**, *115*, D22111. [CrossRef]
20. Zou, X.; Liu, H.; Kuo, Y. Occurrence and detection of impact multipath simulations of bending angle. *Q. J. R. Meteorol. Soc.* **2019**, *145*, 1690–1704. [CrossRef]
21. Liu, H.; Kuo, Y.-H.; Sokolovskiy, S.; Zou, X.; Zeng, Z.; Hsiao, L.-F.; Ruston, B.C. A quality control procedure based on bending angle measurement uncertainty for radio occultation data assimilation in the tropical lower troposphere. *J. Atmos. Ocean. Technol.* **2018**, *35*, 2117–2131. [CrossRef]
22. Yang, S.; Zou, X. Relationships of along-the-track local variations of GPS ro impact parameter to strong local vertical gradient of wet refractivity in the Tropics. *Sci. China Earth Sci.* **2021**, *64*, 2015–2026. [CrossRef]
23. Zhang, H.; Shao, H.; Ruston, B.; Braun, J.J. Impact study of increased radio occultation observations during the ROMEX period using JEDI and the GFS atmospheric model. *Atmos. Meas. Tech.* **2025**, *18*, 6167–6184. [CrossRef]
24. Zhang, H. *Intercomparison of GNSS RO Quality Control Methods in NWP*; ROM SAF CDOP 4 Visiting Scientist Report 41; ROM SAF: Copenhagen, Denmark, 2024; 55p.
25. Zou, X.; Wang, B.; Liu, H.; Anthes, R.A.; Matsumura, T.; Zhu, Y.-J. Use of GPS/MET refraction angles in three-dimensional variational analysis. *Q. J. R. Meteorol. Soc.* **2000**, *126*, 3013–3040. [CrossRef]
26. Zou, X.; Liu, H.; Anthes, R.A.; Shao, H.; Chang, J.C.; Zhu, Y.-J. Impact of CHAMP radio occultation observations on global analysis and forecasts in the absence of AMSU radiance data. *J. Meteorol. Soc. Jpn. Ser. II* **2004**, *82*, 533–549. [CrossRef]
27. Liu, H.; Zou, X. Improvements to a GPS radio occultation ray-tracing model and their impacts on assimilation of bending angle. *J. Geophys. Res. Atmos.* **2003**, *108*, 4548. [CrossRef]
28. Eyre, J. Assimilation of radio occultation measurements into a numerical weather prediction system. *ECMWF Tech. Memo.* **1994**, *34*, 199. [CrossRef]
29. Healy, S.B. Radio occultation bending angle and impact parameter errors caused by horizontal refractive index gradients in the troposphere: A simulation study. *J. Geophys. Res. Atmos.* **2001**, *106*, 11875–11889. [CrossRef]
30. Xie, F.; Wu, D.L.; Ao, C.O.; Mannucci, A.J.; Kursinski, E.R. Advances and limitations of atmospheric boundary layer observations with GPS occultation over Southeast Pacific Ocean. *Atmos. Chem. Phys.* **2012**, *12*, 903–918. [CrossRef]
31. Kuo, Y.-H.; Wee, T.-K.; Sokolovskiy, S.; Rocken, C.; Schreiner, W.; Hunt, D.; Anthes, R.A. Inversion and error estimation of GPS Radio Occultation Data. *J. Meteorol. Soc. Jpn. Ser. II* **2004**, *82*, 507–531. [CrossRef]
32. Ho, S.; Kirchengast, G.; Leroy, S.; Wickert, J.; Mannucci, A.J.; Steiner, A.; Hunt, D.; Schreiner, W.; Sokolovskiy, S.; Ao, C.; et al. Estimating the uncertainty of using GPS radio occultation data for Climate Monitoring: Intercomparison of Champ Refractivity Climate Records from 2002 to 2006 from different data centers. *J. Geophys. Res. Atmos.* **2009**, *114*, D23. [CrossRef]
33. Kuo Hersbach, H.; Bell, B.; Berrisford, P.; Hirahara, S.; Horányi, A.; Muñoz-Sabater, J.; Nicolas, J.; Peubey, C.; Radu, R.; Schepers, D.; et al. The ERA5 global reanalysis. *Q. J. R. Meteorol. Soc.* **2020**, *146*, 1999–2049. [CrossRef]
34. Hoffmann, L.; Günther, G.; Li, D.; Stein, O.; Wu, X.; Griessbach, S.; Heng, Y.; Konopka, P.; Müller, R.; Vogel, B.; et al. From ERA-Interim to ERA5: The considerable impact of ECMWF's next-generation reanalysis on Lagrangian transport simulations. *Atmos. Chem. Phys.* **2019**, *19*, 3097–3124. [CrossRef]
35. Fleming, E.L.; Chandra, S.; Barnett, J.J.; Corney, M. Zonal mean temperature, pressure, zonal wind and geopotential height as functions of latitude. *Adv. Space Res.* **1990**, *10*, 11–59. [CrossRef]
36. Zou, X.; Vandenberghe, F.; Wang, B.; Gorbunov, M.E.; Kuo, Y.-H.; Sokolovskiy, S.; Chang, J.C.; Sela, J.G.; Anthes, R.A. A ray-tracing operator and its adjoint for the use of GPS/MET refraction angle measurements. *J. Geophys. Res. Atmos.* **1999**, *104*, 22301–22318. [CrossRef]
37. Smith, E.; Weintraub, S. The constants in the equation for atmospheric refractive index at radio frequencies. *Proc. IRE* **1953**, *41*, 1035–1037. [CrossRef]
38. Ao, C.O.; Waliser, D.E.; Chan, S.K.; Li, J.; Tian, B.; Xie, F.; Mannucci, A.J. Planetary boundary layer heights from GPS radio occultation refractivity and humidity profiles. *J. Geophys. Res. Atmos.* **2012**, *117*, D16117. [CrossRef]
39. Yang, S.; Zou, X.; Anthes, R. Raytracing Simulated GPS Radio Wave Propagation Paths Experiencing Large Disturbances When Going through the Top of the Sub-Cloud Layer. *Remote Sens.* **2021**, *13*, 4693. [CrossRef]
40. Feng, X.; Xie, F.; Ao, C.O.; Anthes, R.A. Ducting and biases of GPS radio occultation bending angle and refractivity in the moist lower troposphere. *J. Atmos. Ocean. Technol.* **2020**, *37*, 1013–1025. [CrossRef]
41. Xie, F.; Wu, D.L.; Ao, C.O.; Kursinski, E.R.; Mannucci, A.J.; Syndergaard, S. Super-refraction effects on GPS radio occultation refractivity in marine boundary layers. *Geophys. Res. Lett.* **2010**, *37*, L11805. [CrossRef]

42. Paluch, I.R.; Lenschow, D.H. Stratiform Cloud Formation in the Marine Boundary Layer. *J. Atmos. Sci.* **1991**, *48*, 2141–2158. [CrossRef]
43. Rahn, D.A.; Garreaud, R. Marine boundary layer over the subtropical southeast Pacific during vocals-rex—Part 1: Mean structure and diurnal cycle. *Atmos. Chem. Phys.* **2010**, *10*, 4491–4506. [CrossRef]
44. Rahn, D.A.; Garreaud, R. Marine boundary layer over the subtropical southeast Pacific during vocals-rex—Part 2: Synoptic variability. *Atmos. Chem. Phys.* **2010**, *10*, 4507–4519. [CrossRef]
45. Winning, T.E.; Chen, Y.-L.; Xie, F. Estimation of the marine boundary layer height over the central North Pacific using GPS Radio Occultation. *Atmos. Res.* **2017**, *183*, 362–370. [CrossRef]
46. Zhou, X.; Kollias, P.; Lewis, E.R. Clouds, precipitation, and marine boundary layer structure during the magic field campaign. *J. Clim.* **2015**, *28*, 2420–2442. [CrossRef]

Disclaimer/Publisher's Note: The statements, opinions and data contained in all publications are solely those of the individual author(s) and contributor(s) and not of MDPI and/or the editor(s). MDPI and/or the editor(s) disclaim responsibility for any injury to people or property resulting from any ideas, methods, instructions or products referred to in the content.